Intermediate-depth earthquakes in southern Spain and Alboran Sea

Carolina López-Sánchez [a,*], Elisa Buforn [a,b], Simone Cesca [c], Lucía Lozano [d], Carlos Sanz de Galdeano [e], Maurizio Mattesini [a,b], Agustín Udías [a], Juan Vicente Cantavella [d]

[a] *Departamento de Física de la Tierra y Astrofísica, Universidad Complutense de Madrid, Madrid, Spain*
[b] *Instituto de Geociencias (UCM-CSIC), Madrid, Spain*
[c] *Helmholtz-Zentrum Potsdam Deutsches GeoForschungsZentrum, Potsdam, Germany*
[d] *Spanish Seismic Network, Instituto Geográfico Nacional, Madrid, Spain*
[e] *Former member of Instituto Andaluz de Ciencias de la Tierra (CSIC – Univ. Granada), Spain*

ARTICLE INFO

ABSTRACT

A striking feature of the seismicity in the Ibero-Maghrebian region is a narrow band of intermediate-depth earthquakes (50 < h < 100 km) beneath the western part of the Alboran Sea, with epicenters following a NNE-SSW alignment. The origin and characteristics of this seismicity are debated, and an accurate analysis of this seismic scenario is provided despite the low to moderate magnitude of these earthquakes. In this study, we collect 20 years of seismic data from permanent and temporary installations and reprocess these data with the aid of advanced seismological techniques, including non-linear probabilistic relocation with a 3D-Earth velocity model and a probabilistic moment tensor inversion scheme, to shed new light on intermediate-depth seismicity in Southern Spain and the Alboran Sea. We relocated 238 intermediate-depth earthquakes (M ≥ 3) using a nonlinear probabilistic approach and a recent regional 3D tomography lithospheric velocity model for the Alboran-Betic Rif Zone. Maximum likelihood hypocenters confirm the NNE-SSW distribution in a depth range between 50 and 100 km, depicting three clusters of epicenters with a seismic gap that may be correlate to the boundary between the sunken slabs of the Iberian and African plates around Gibraltar. We simultaneously determined the focal mechanisms of 25 mb > 3.9 earthquakes using P-waves and moment tensors by fitting body-wave amplitude spectra and waveform cross-correlations. We performed an accurate resolution study by repeating the inversion using different 1-D velocity models. The results show predominant horizontal T axes with a rotation on the direction from N*E*-SW in southern Spain to E-W near the African coast. The distribution of intermediate-depth earthquakes and their source geometries provide new evidence of the seismotectonic complexity of the region, which is possibly controlled by the stopping or slowing down of subduction.

1. Introduction

The Alboran Sea is located between the Iberian Peninsula and northern Morocco in the western part of the Mediterranean Sea (Fig. 1) at the plate boundary between Eurasia and Africa. Its origin is the opening of the Algero-Provençal Basin that occurred from the end of the Oligocene-early Aquitanian to the end of the Burdigalian, perhaps the beginning of the Langhian, in a process that lasted approximately 10 My, from ~24 to ~14 My (Fig. 2; Sanz de Galdeano, 1990). The process of the formation of this basin, where the Alboran Sea corresponds to its western end, caused a great break in the region, forming domains that were progressively dispersed in several directions, some to the east, others to the south, and still others to the west. At this stage, the Betic-Rif

Internal Zone domain was progressively pushed westwards. This Internal Zone was situated initially at the NW and W parts of the future Algerian Basin that then began to open (Fig. 2). Owing to this process of opening progressively occupying more space, the Internal zone was pushed and began its westward drift to later collide with the Betic External Zone, and immediately after collided with the Riffian External Zone and then formed the Rif Mountains. In the drift process, the Internal Zone was partially superposed to a part of the Iberian crust and also to a part of the African crust (in the proximities of northern Morocco). Both sectors of crusts began to sink, that is, began to subduct. Morphologically, this area where occurred the overthrusts corresponds to the present Gibraltar Arc. Andrieux et al. (1971) and Udías and López-Arroyo (1972) were the first to link the formation of the Gibraltar Arc to

---

* Corresponding author.
  E-mail address: caroll04@ucm.es (C. López-Sánchez).

subduction.

As a consequence of these processes, southern Iberia, the Alboran Sea and northern Morocco form a very tectonically complex region, where the plate boundary is a wide deformation zone. Evidence of this complexity its seismicity is characterized by a continuous occurrence of moderate earthquakes (M < 5) at shallow (h < 40 km) and intermediate depths (40 km < h < 150 km) and occasionally events at very deep depths of ~650 km (Fig. 3) (http://www.ign.es/web/ign/portal/sis-catalogo-terremotos). The occurrence of earthquakes at intermediate depths in the Gulf of Cadiz, Alboran Sea and northern Morocco was recognized early and is currently well-known (Munuera, 1963; Udías et al., 1976; Hatzfeld, 1978; Hatzfeld and Frogneux, 1981; Grimison and Chen, 1986; Buforn et al., 1988a,b, 1995, 1997; Morales et al., 1999). The distribution of intermediate-depth epicenters is substantially different to the east and west of the Strait of Gibraltar (SG). In the Gulf of Cadiz, west of the SG, their epicenters are elongated along the E-W and NW-SE (Fig. 3) directions, similar to those of shallow events. This spatial pattern can be explained in terms of plate boundary convergence. Furthermore, focal depths for offshore earthquakes are poorly constrained due to poor azimuthal station coverage (Cabieces et al., 2020). However, east of Gibraltar, in the western part of the Alboran Sea (marked as a square in Fig. 3), intermediate-depth earthquakes (focal depths less than 150 km) are distributed following a narrow arc parallel to the SG, which does not agree with the distribution of the overlying shallow earthquakes. Depth estimates are better constrained in this domain because the station density and network coverage are higher than to the west of SG. Shallow earthquakes in the Alboran Sea are mostly located east of the intermediate-depth events, with the most active zone between Alhoceima (northern Morocco) and Alboran Island, where the largest earthquakes have occurred. These earthquakes are the 2004 Mw 6.3 Alhoceima (Morocco) and the 2016 Mw 6.4 Alboran Sea earthquakes (Fig. 3), both with shallow depths (h < 10 km) (Aït Brahim et al., 2004; Jabour et al., 2004; Stich et al., 2005; Buforn et al., 2017; Medina and Cherkaoui, 2017; Galindo-Zaldivar et al., 2018; Kariche et al., 2018; Gràcia et al., 2019; Stich et al., 2020). These earthquakes are well correlated to the geological faults of this zone.

Other evidence of regional complexity is the occurrence of very deep earthquakes (h > 600 km) located south of Granada, the largest recorded, those of 1954, M = 7.8 (gray triangle in Fig. 3) and the 2010, Mw 6.3 (black triangle in Fig. 3; Buforn et al., 2011; Mancilla et al., 2012; Bezada and Humphreys, 2012). No seismicity is reported between depths of 150 and 600 km (Hodgson and Cock, 1956; Chung and Kanamori, 1976; Udías et al., 1976; Grimison and Chen, 1986; Buforn et al., 1991, 1997, 2011).

This complex seismicity distribution is controlled by the interaction of the Eurasian and African plates, which have a complex, not well-defined continental plate margin. The origin of intermediate-depth earthquakes in the Alboran Sea is still under discussion. Over the years, different mechanisms have been proposed, including continued subduction (Hatzfeld and Frogneux, 1981; Morales et al., 1999; Casado et al., 2001; Gutscher et al., 2002, 2012), but recent studies (Pedrera et al., 2011; Buforn et al., 2016; Sun and Bezada, 2020) propose that subduction is not currently active and that its seismicity corresponds to the present NNW-SSE compression existing between Iberia and Africa. Other proposed origins include delamination of the continental lithosphere (Grimison and Chen, 1986; Seber et al., 1996; Mezcua and Rueda, 1997; Calvert et al., 2000), extensional collapse of the continental lithosphere (Platt and Vissers, 1989) and rollback of a dipping slab from different subduction geometries (Spakman and Wortel, 2004; de Lamotte et al., 2009; Van Hinsbergen et al., 2014; Carminati et al., 2012;
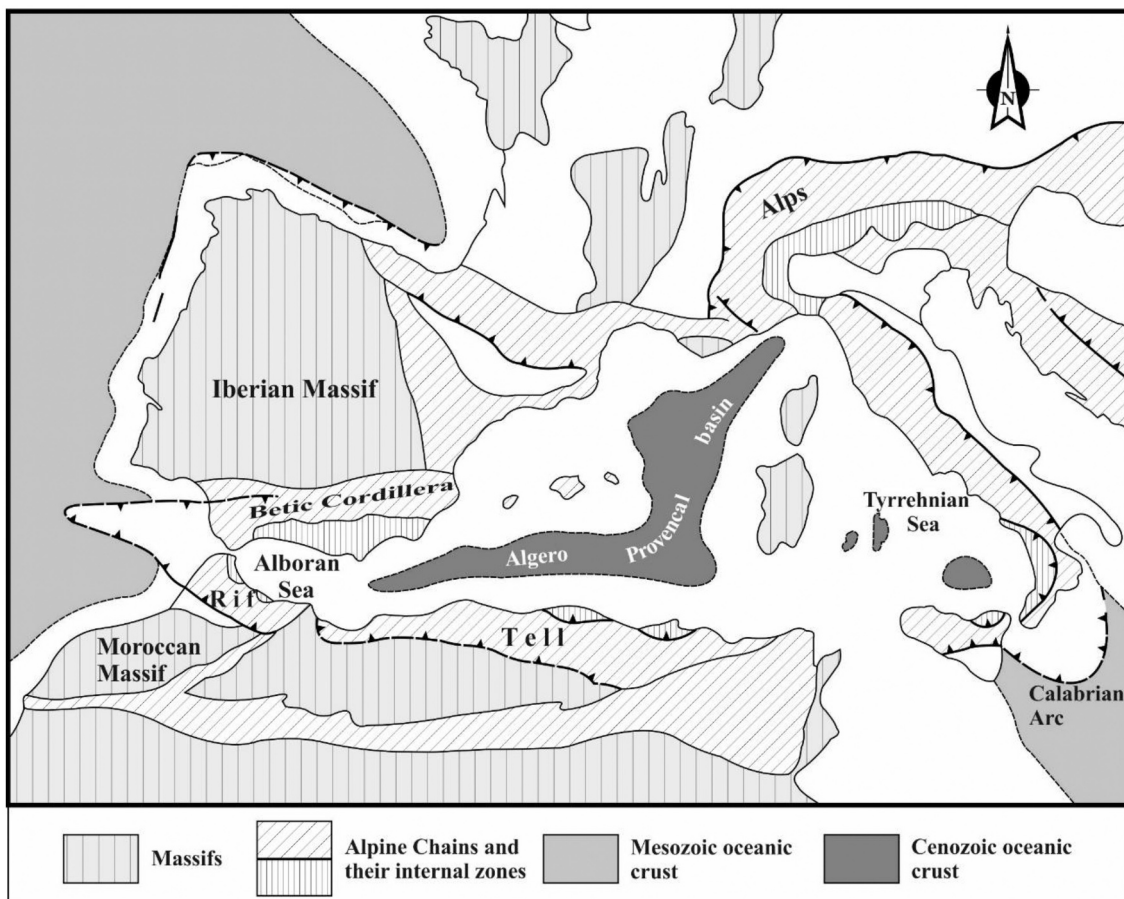

Fig. 1. Regional location of the Alboran Sea in the western Mediterranean Sea. Main geological units and features are showed.

Vergés and Fernàndez, 2012). The *E*-W extension found in the shallow part of the crust in the Alboran Sea may be explained using different tectonic models, such as some kind of complex shallow subduction or delamination process (Buforn et al., 1997, 2016; Mancilla et al., 2013; Levander et al., 2014). Tomographic studies coincide in the identification of a positive speed anomaly in the upper mantle dipping beneath the Alboran Sea, although its origin and geometry are debated (Blanco and Spakman, 1993; Spakman and Wortel, 2004; Amaru, 2007). Recent tomographic studies have shown a narrow steeply dipping curved slab (Bezada et al., 2013; Van Hinsbergen et al., 2014; Palomeras et al., 2014). It is still debated whether the slab is detached (Piromallo and Morelli, 2003; Palomeras et al., 2014) or connected to the surface (Spakman and Wortel, 2004; Bezada et al., 2013). This is hardly resolved, given that tomographic models do not have resolution at shallow depths (50 to 100 km). Two recent studies have provided the most new and reliable information: Sun and Bezada (2020) relocated more than 900 intermediate-depth earthquakes between 1997 and 2017, and Santos-Bueno et al. (2019) relocated 145 events for the 2007–2012 period and estimated the fault-plane solutions of 42 of them using P-wave first motion.

The objective of our study is to extend these studies, by carrying out a detailed analysis of intermediate-depth seismicity. In our study, we obtain 238 absolute relocations of earthquakes for the period 2000–2020 versus 58 of Sun and Bezada (2020) and focal mechanism for 25 events (M > 3.9) from moment tensor inversion while Santos-Bueno et al. (2019) have used P-wave first motion. We relocated the earthquakes using a nonlinear probabilistic search, accounting for a regional 3D velocity model (*NonLinLoc*, Lomax et al., 2000). The use of a nonlinear probabilistic approach, which provides "optimal" hypocenters and complete information on location uncertainties, along with the use of realistic 3-D lithospheric models that allow the inclusion of propagation effects of highly heterogeneous velocity structures within a region, is a powerful tool to improve the hypocentral parameters and better constrain the seismicity distribution (Buforn et al., 2017; Lozano et al., 2020). Focal mechanisms and moment tensors are obtained based

on first-motion polarities and fit of waveforms and spectra, respectively. Moment tensor inversion is performed using a Bayesian optimizer (*GROND*, Heimann et al., 2018), which provides source parameters, including non-double-couple components, and their uncertainties.

2. Hypocentral relocation

An accurate determination of the geometry of seismic sources of intermediate earthquakes in the Alboran Sea is important to better constrain the focal mechanisms. Hypocentral relocation was performed using the *NonLinLoc* software package. To take into account the complex regional lithospheric structure, we use a 3D velocity model (El Moudnib et al., 2015) instead of a simplified 1D model, which allows us to account for propagation effects in highly heterogeneous velocity structures within the Alboran Sea region. *NonLinLoc* performs a nonlinear probabilistic search for a seismic hypocenter allowing travel time within a 3-D grid to be calculated. This method follows the inversion approach of Tarantola and Valette (1982), which provides "optimal" hypocenters and an estimate of the posterior probability density function (PDF) for the location of the spatial hypocenter and more reliable location uncertainties than linearized classical inversions. The 3D model used in this study covers the crust and upper mantle of the Alboran-Betic Rif Zone, which was proposed based on recent high-resolution P-wave tomography (El Moudnib et al., 2015). Using an accurate 3D model allows us to account for differences in the travel times of seismic waves within the different crustal domains reported for this region (Gómez de la Peña et al., 2018). The 3-D model was parametrized as a regular grid volume of constant velocity cells of $20 \times 20 \times 4$ km^3 in the x, y and z directions. For the travel-time calculations, we considered a finer grid of $1 \times 1 \times 1$ km^3 obtained by interpolation from the original model and extended to a depth of 200 km with the IASP91 global model (Kennett and Engdahl, 1991). To take into account S arrivals, we assumed a constant vp/vs ratio of 1.73 obtained from the Wadati diagram (Wadati, 1933) of a set of 960 intermediate-depth earthquakes (M $\geq$ 2) recorded in the region between 2000 and 2020. Theoretical P- and S-wave travel times from
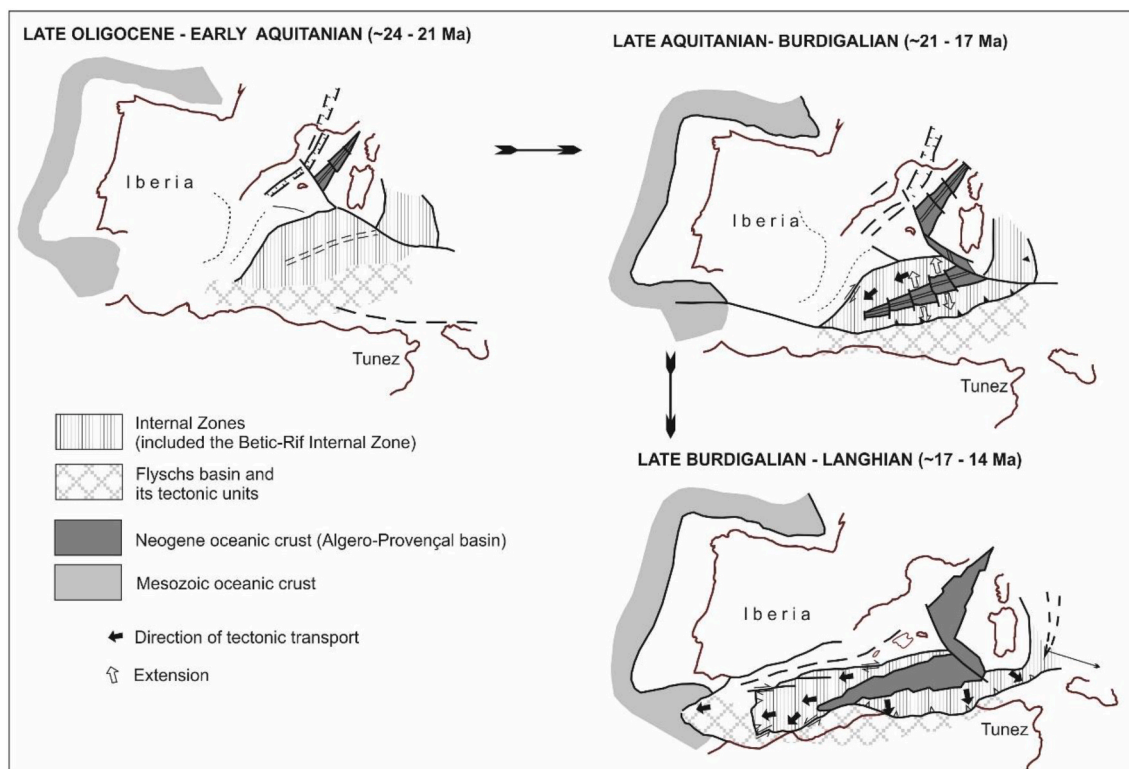

Fig. 2. Kinematic reconstruction of the opening of the Algerian Basin, after Sanz de Galdeano (1990).
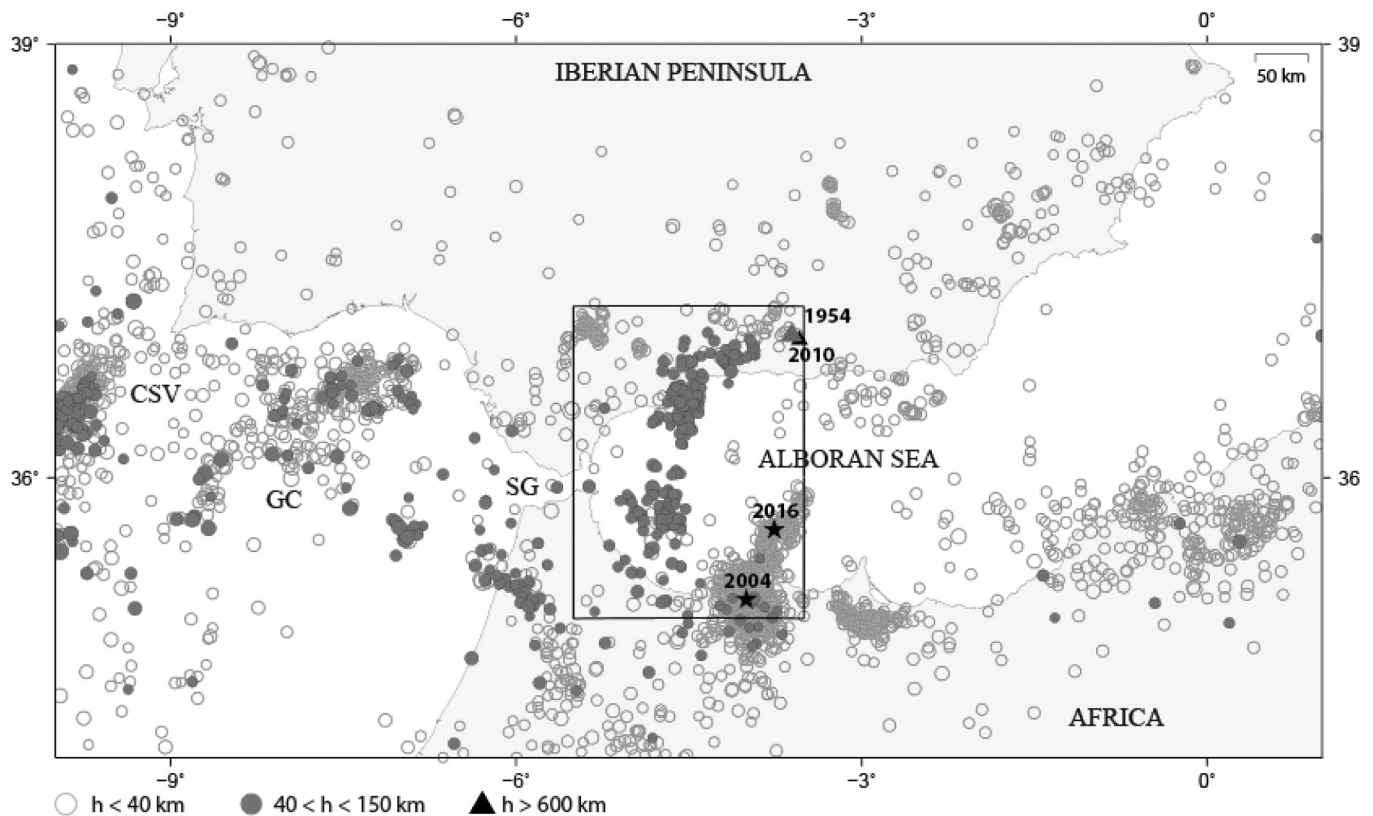
Fig. 3. Epicenters for the 2000–2020 period with M ≥ 3 (http://www.ign.es/web/ign/portal/sis-catalogo-terremotos). Epicenters of the 1954 and 2010 deep earthquakes are the gray and black triangle, respectively. Black stars denote the 2004 and 2016 shallow earthquakes. The rectangle shows the region studied in this paper. CSV: Cape Saint Vincent. GC: Gulf of Cadiz. SG: Strait of Gibraltar.

each 3-D grid node to each station were calculated using finite differences approximation of Huygens' principle (Podvin and Lecomte, 1991). To compute the probabilistic solution, we used the equal differential-time (EDT) likelihood function, which is very robust in the presence of outliers in the data (Lomax, 2005). The oct-tree importance sampling method, which is faster than the conventional grid search (Lomax and Curtis, 2001), was applied as the search algorithm for the PDF evaluation.

We applied this methodology to relocate earthquakes with moderate magnitudes (M ≥ 3) and intermediate depths (40 to 110 km) in the catalog of the Instituto Geográfico Nacional (Instituto Geográfico Nacional (IGN), 2021; http://www.ign.es/web/ign/portal/sis-catalogo-terremotos) for the 2000–2020 period in the western Alboran Sea (35.0–37.2°N, 3.7–5.4°W) (Fig. 3, rectangle). An initial set of 286 earthquakes in the IGN catalog were selected using these criteria. The data correspond to 12,127 total P- and S-wave first arrivals (secondary phases are not considered) from the IGN catalog, for a total of 151 seismic stations from permanent and temporary networks (Fig. 4) within the region covered by our 3-D velocity grid. These networks are ES, Spanish Seismic Network (doi: https://doi.org/10.7914/SN/ES); PM, Portuguese National Seismic Network (doi: https://doi.org/10.7914/SN/PM); WM, Western Mediterranean Seismic Network (doi: 10.14470/JZ581150); IG, Southern Spain Broadband seismic network; LX, Universidade de Lisboa (doi: https://doi.org/10.7914/SN/LX); DZ, Centre de Reserche en Astronomie, Astrophysique et Geophysique de Algeria; SPGM, Service du Physique du Globe, Rabat, Morocco; MN, MEDNET (doi: 10.13127/SD/fBBBtDtd6q); X1, UCM, Universidad Complutense de Madrid. Fig. 4 shows the percentage of earthquakes to which each station has contributed (for more details, see Supplementary Material Table S1). The stations with lower contributions correspond to temporary stations available for one or two months only, while

permanent stations have larger contributions (with the darkest colors in Fig. 4). This figure highlights the higher density of stations in southern Spain versus the low number of permanent seismic stations in northern Africa. This is indicated by a slight increase in the hypocentral location uncertainties when approaching Morocco (Supplementary Material Fig. S1 and Table S1). Events with few readings (less than 20 readings and 8 P-S pairs) and observations with large time residuals (>2.0 s) were removed, and we considered only well-constrained solutions. With these criteria, we reduced the dataset to 238 earthquakes, with a mean azimuthal gap of approximately 140°. The large number of events allowed us to derive robust station corrections, and station delays were included in the location process by means of the average of the phase residuals for P- and S-waves, including the station delays in a second run. From the final set of events, 11 events have been relocated at shallow depths (h < 40 km), with average depth uncertainties of 15 km, and are no longer considered intermediate-depth earthquakes. Two of the shallow earthquakes are located at the Malaga coast, around 34 to 39 km depth (± 5 km), similar to the IGN catalog locations (40–43 ± 5 km). However, we removed them from Fig. 5 and the discussion to keep consistency in our analysis of the intermediate-depth seismicity. The remaining nine shallow events correspond to earthquakes mostly located along the Moroccan coast, except for one in southern Alboran sea. We have carefully checked these events, comparing their S-P times with the S-P of deeper earthquakes, with similar epicentral locations, at certain common stations. Inconsistencies in the S-P values, few available P-S picks, large azimuthal gaps and large depth errors of most of them, lead us to conclude that these earthquakes may be mislocated in depth. Thus, we discarded them for later discussion.

Relocated seismicity is distributed in a narrow NNE-SSW band beneath the western part of the Alboran Sea, bending ENE-WSW beneath the coast of Spain. We observe a lateral variation in the seismicity rate
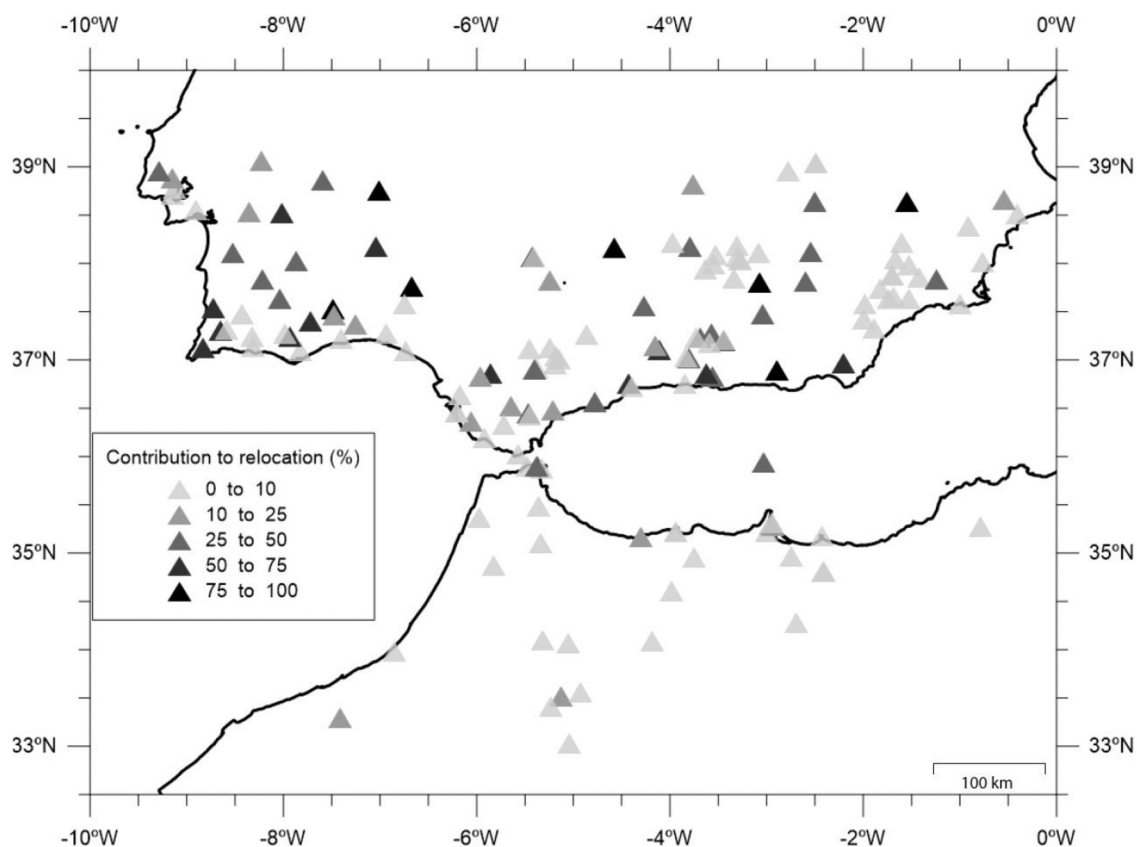
Fig. 4. Contribution of each station to the relocation process (in % relative to the total number of relocated events, Supplementary Material Table S1). The stations used to belong to the following seismic networks: ES, Spanish Seismic Network (doi: https://doi.org/10.7914/SN/ES); PM, Portuguese National Seismic Network (doi: https://doi.org/10.7914/SN/PM); WM, Western Mediterranean Seismic Network (doi: 10.14470/JZ581150); IG, Southern Spain Broadband seismic network (r); LX, Universidade de Lisboa (doi: https://doi.org/10.7914/SN/LX); DZ, Centre de Reserche en Astronomie, Astrophysique et Geophysique of Algeria; SPGM, Service du Physique du Globe, Rabat, Morocco; MN, MEDNET (doi: 10.13127/SD/fBBBtDtd6q); X1, UCM, Universidad Complutense de Madrid.

along this curved profile, almost parallel to the Gibraltar Arc, with an alternation of seismically active regions and aseismic regions (Fig. 5a). A small seismic gap is observed around latitude 36°N. We identify two spatial clusters north of this gap, which we refer to as Clusters A1 and A2, and one to the south, namely, Cluster A3. Cluster A1 is located inland, with epicenters extending in the E-W direction from 3.9°W to 4.6°W and latitude 37.0°N to 36.75°N. Clusters A2 (36.25°N-36.75°N) and A3 (35.9°N to 35.3°N) have N-S orientations extending from 4.4°W to 5.2°W. In Fig. 5b, we show a vertical N-S cross-section of hypocenters together with their depth error bars. The maximum depth is approximately 100 km, and the hypocentral depths smoothly decrease in Cluster A2 to the north, in the direction of the Spanish coast. In Cluster A3, we observe a similar although less marked behavior, with focal depth decreasing from latitude 36°N to the south. In addition, it is observed a depth increasing from west to east in A2 and A3. The depth errors are larger for Cluster A3 due to the lower number of local stations and the asymmetric distribution of the seismic network. The deepest earthquakes are found in both A2 and A3 clusters, close to the central aseismic region. In Cluster A1, the hypocenters are shallower, between 40 and 70 km, except for three earthquakes with a greater depth uncertainty (Fig. 5b). Hypocenters and their uncertainties are given in Supplementary Material Table S2. The uncertainties are represented by the 90% confidence depth interval (ErrZ), ellipse semi-major and semi-minor axes (Smajax and Sminax, respectively), and the strike of the semi-major axis. Fig. 5c shows a vertical E-W cross section of hypocenters, which highlights that the maximum depth (approximately 100 km) is reached between 4.7°W and 4.5°W (Eastern part of Clusters A2 and A3) and that the depth decreases when we move to the east and west. The

figure also shows that the uncertainties are smaller for earthquakes inland and offshore near the Spanish coast and become larger toward the African coast due to the worse station coverage and lower available P-S pairs. Epicentral uncertainties range between 1 and 13 km in the southern Alboran Sea, 1–10 km close to the coast of Spain and 1–8 km onshore. Depth uncertainty ranges are 4–25 km, 2–13 km and 2–10 km, respectively, in the same regions. The uncertainty ellipsoids are typically elongated WNW-ESE or ENE-WSW, implying larger uncertainties in longitude. The root mean square (RMS) has values between 0.19 and 0.62 s (Supplementary Material Table S2).

The comparison between the relocations obtained in this study and those of the IGN catalog (Supplementary Material Fig. S1), using the linear algorithm *LocSAT* (Bratt and Bache, 1988) and a 1D model for the whole Iberian region (Martínez-Solares, 1995), shows a significant improvement. For the epicenter, the major and minor ellipsoid axes (Supplementary Material Fig. S2 and Table S2) are reduced (86% and 93%, respectively), on average by ~1 km (http://www.ign.es/web/ign/portal/sis-catalogo-terremotos). The largest improvement (~9 km) is found for earthquakes in Cluster A3. Depth uncertainties decrease for 168 events (74%), with differences up to ~24 km (Supplementary Material Fig. S2 and Table S2). Our results display an overall eastward shift of the epicenters, ranging between 1 and 13 km; epicenters with a larger shift are those onshore and off the coast of Spain. The depth of 39 (91%) onshore earthquakes is reduced between 1 and 15 km, while for offshore earthquakes, it increases for 130 (71%) events between 1 and 30 km (see Supplementary Material Table S2).
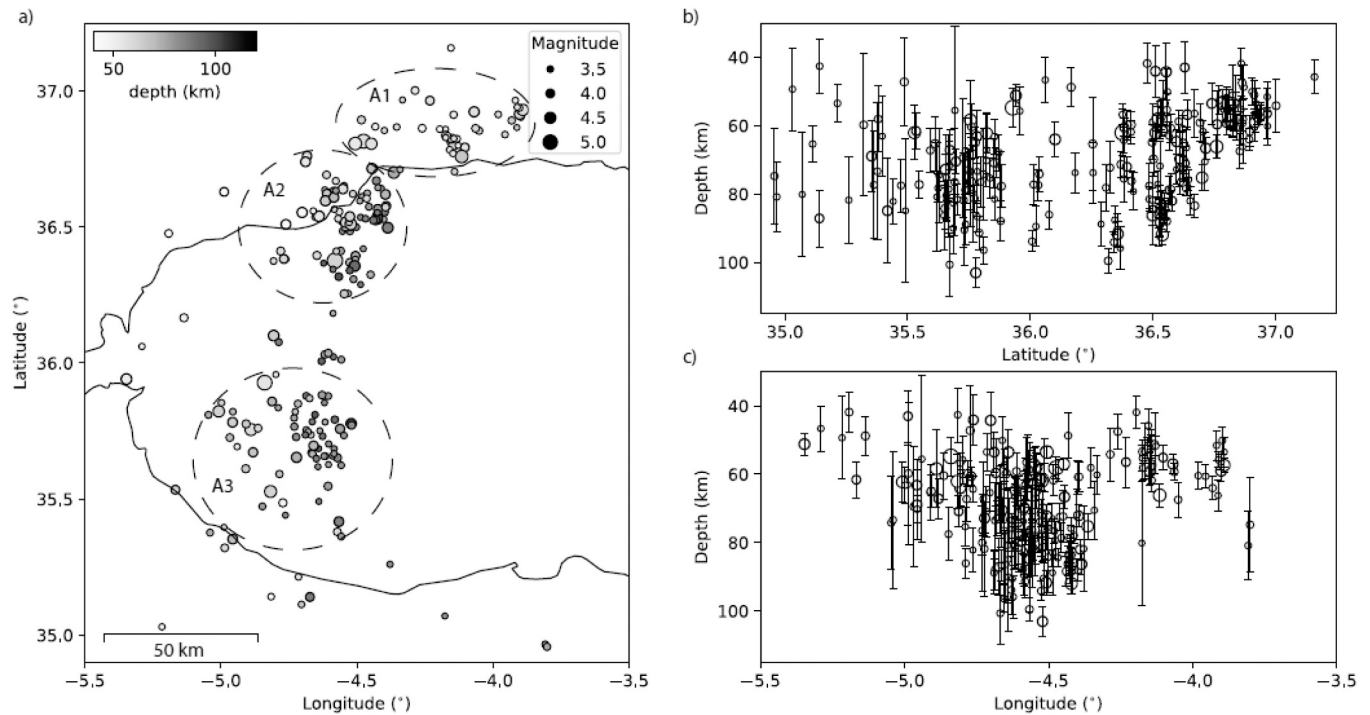
Fig. 5. Relocated hypocenters of M ≥ 3.0 intermediate-depth earthquakes (h > 40 km) that occurred in the western Alboran region (2000–2020) using the *NonLinLoc* algorithm (Lomax et al., 2000) and a regional lithospheric 3D velocity model (El Moudnib et al., 2015). On the right, latitude (north-south) and longitude (east-west) depth profiles with depth uncertainty bars are shown. Dashed circles represent different clusters (A1, A2 and A3).

3. Focal mechanisms

We selected 25 earthquakes out of 238 relocated events that occurred between 2002 and 2020 with magnitude 3.9 ≤ mb ≤ 4.8 (IGN catalog) and focal depth varying from 50 to 110 km after relocation (Supplementary Material Table S2). These earthquakes have well-constrained hypocenters, with location errors of less than 5 km for the epicenter and between 2 and 6 km for depth (earthquakes E1, E3 and E17 have depth errors of 10, 11 and 8 km, respectively, Supplementary Material Table S2). We investigated their seismic sources using two different approaches. First, we obtained the fault-plane orientation using a P-wave first-motion (FM) method. Next, we performed a moment tensor inversion using a probabilistic inversion approach to obtain a deviatoric moment tensor (MT). Comparing the results of the two independent methods allows us to evaluate their quality. We used 113 stations at regional distances (x < 800 km) from permanent and temporary networks (Supplementary Material Fig. S3). The number of stations used for each earthquake changes depending on their availability and the method used: between 6 and 31 stations for the polarity method and between 4 and 34 stations for the MT inversion. These data correspond to the following networks: ES (Spanish National; doi: https://doi.org/10.7914/SN/ES), WM (Western Mediterranean; doi: 10.14470/jz581150), PM (Portuguese National; doi: https://doi.org/10.7914/SN/PM), GSN-IU (Global Seismograph Network; doi: https://doi.org/10.7914/SN/IU) and IP (Instituto Superior Tecnico Broadband) permanent seismic networks; and they correspond to the following deployments: the TopoIberia-Iber Array (doi: https://doi.org/10.7914/SN/IB), TEDESE, PICASSO (doi: https://doi.org/10.7914/SN/XB_2009) and Hire-II (doi: 10.14470/8 W7568280780) deployments (Supplementary Material Fig. S3).

For the polarity method, we used *MECSTA* software with stations located at epicentral distances below 800 km (Buforn and Udías, 1984; Udías and Buforn, 1988). This method is based on a probabilistic model developed by Brillinger et al. (1980) that provides the fault plane orientation together with the T and P axes, an estimation of their errors, and the score for each solution. The score is defined as the ratio of correct polarities out of the total number of observations. We used a lithospheric model with a gradient velocity to estimate the take-off angles (Buforn and Udías, 1984). Only observations with a clear P-wave arrival on vertical components have been used, with an average of 16 polarities per earthquake (Supplementary Material Table S3).

The moment tensor inversion is performed using *GROND* software to fit ground displacements and spectra. Displacement waveforms are obtained after deconvolution of the instrumental transfer function, rotation of the horizontal components to radial and transverse components, and bandpass filtering. *GROND* has been used in several other studies, even in the same region (Hensch et al., 2019; Walter et al., 2019; Cabieces et al., 2020). For permanent stations, we simultaneously fitted the displacement waveforms of the P and S phases in the vertical and transverse components, respectively, as well as their corresponding amplitude spectra. For temporary installations, where we could not verify the reliability of the instrumental response, we fit the displacement traces only by cross-correlation. A similar approach has been used for a recent study offshore Spain (Cesca et al., 2021). Given the low magnitude of the selected earthquakes, we used only stations with epicentral distances up to 300 km. Furthermore, given the intermediate depth of the earthquakes, with seismic signals characterized by clear P- and S-wave onsets but low-amplitude surface waves, we used a 6 s time window for the P phases in the vertical components and an 8 s time window for the S phases in the transverse components, starting 3 s before the manually picked phase arrivals in both cases. The frequency band for each earthquake was selected to maximize the signal-to-noise ratio. In most cases, we used a bandpass of 0.5–2 Hz. In some cases, when the microseismic noise reduced the signal-noise ratio, we increased the bandpass to 1–3 Hz. We further increased the frequency bandpass to 1.5–4 Hz in only one case. We manually checked all waveforms and removed a few traces with high noise levels, data gaps or mismatches among theoretical and picked arrival times. As a result, *GROND* provides the scalar seismic moment (M_0), moment magnitude (M_w), moment tensor components, centroid location and depth and

centroid time. We restricted the search for the centroid location to within 5 km from the relocated hypocenter. Here, we present the mean MT solution derived from the ensemble of MT solutions obtained by bootstrapping (Heimann et al., 2018). The adopted bootstrap approach provides confidence intervals for all resolved source parameters. Fig. 6 shows an example of an MT inversion result for the E8 earthquake, providing the focal sphere (a), the moment magnitude in gray with a black line in the magnitude of the IGN catalog (b), and selected examples of waveform and spectral fits (c). The fits show the observed (gray lines) and synthetic (black lines) displacement waveforms with a panel that lists the station name (ECEU and EQTA), epicentral distance and azimuth. The bottom panel in the frequency domain shows the comparison between the amplitude spectra of the observed (black filled line) and synthetic (gray filled line) traces.

Synthetic seismograms were computed from Green's functions pre-calculated with the ortho-normalization method *QSEIS* (Wang, 1999). Since the selection of the velocity model could partially bias the moment tensor inversion results (Domingues et al., 2013), we tested the stability of the MT results by repeating the inversion with two different 1-D velocity models, one based on the Crust2.0 database (Bassin et al., 2000) and one proposed by Stich et al. (2003), derived from a selection of local

and regional models (Supplementary Material Fig. S4). We assessed the performance of both velocity models, comparing the average cross-correlation normalized misfit values. Supplementary Material Fig. S5 compares these values for each earthquake, and the velocity model performed similarly. The predictive MT solutions are similar, but the second model (Stich et al., 2003) presents slightly lower misfit values for all earthquakes. For this reason, we only include in the discussion the MT results using the Stich et al. (2003) model.

In this way, we obtained for each earthquake a DC mechanism from first-motion polarities (FM solution in Supplementary Material Fig. S6 and Table S3) and a deviatoric MT solution (MT) from the moment tensor inversion (Supplementary Material Fig. S7 and Table S4). MT solutions were classified as Quality A if they had at least 6 P-wave and 5 S-wave observations, an azimuthal gap for observations lower than 200° and if the number of correct observations over the focal sphere (score) was larger than 70%. If one of these conditions did not hold, the solution is listed as Quality B. We obtained 14 Quality A and 10 Quality B solutions (Supplementary Material Table S5). The comparison of the solutions obtained from FM and MT inversions shows a general agreement, with some differences (differences of P or T axes plunges greater than 30° and/or axes azimuths between 70° and 110° or 250° and 290°)
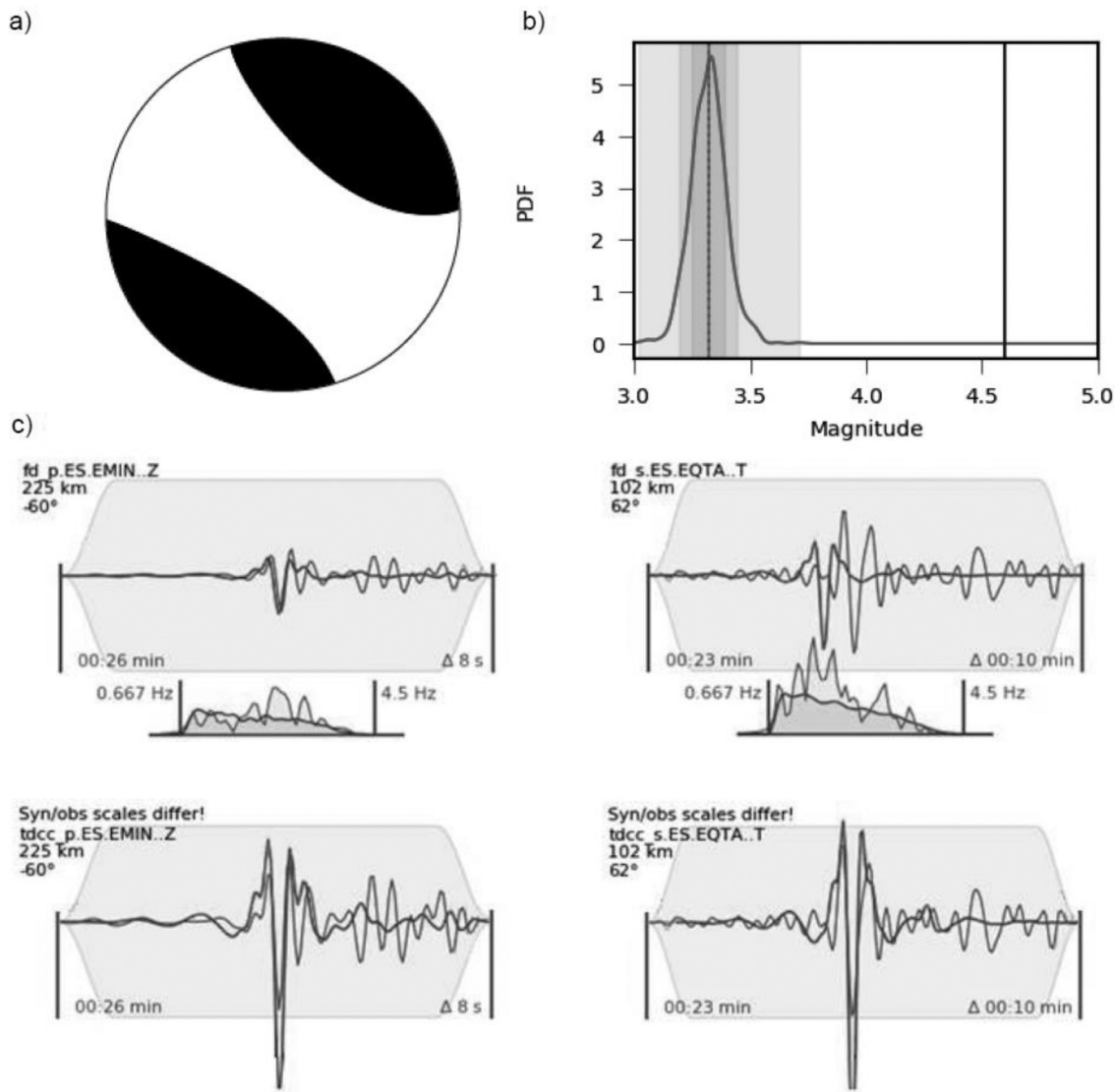

Fig. 6. Moment tensor (MT) inversion results for the E8 earthquake. a) Mean MT solution obtained from the ensemble of MT solutions using *GROND* software (Heimann et al., 2018). b) Magnitude probability density functions. Fits of observed data (gray). c) Synthetic displacement obtained from the best MT.

found for 11 earthquakes (E1, E2, E10, E11, E12, E13, E14, E17, E19, E20 and E22 events).

Fig. 7 shows the best solutions of the selected earthquakes, in some cases corresponding to the FM solution (marked with an asterisk in Table 1) and in the majority of cases to the MT solution (Table 1). For event E1, FM and MT solutions were discarded because of the low number of stations, specifically broadband stations (Supplementary Material Figs. S6 and S7). For events E2 and E10, the MT solution was preferred, as the azimuthal coverage was improved, and the score of the polarity fit was comparable to the P-wave first-motion polarity solution. Some of the MT solutions have large CLVD (Compensated Linear Vector Dipole) components. The orientation of the T axis is poorly resolved for MT solutions with positive CLVD components (events E11, E12, and E17); the same occurs with the orientation of the P axis for MTs with large negative CLVD components (E13, E19, and E20). MT solutions for events E13, E19 and E20 do not fully agree with polarity data (score < 70%), so for these cases, the MT solutions were discarded, and FM solutions were preferred. For events E14 and E22, both FM and MT solutions satisfactorily fit the P-wave polarities (scores >70%), with a good station distribution (gap <155°), so that both solutions could be possible: in these cases, we selected the MT solutions, as they rely on more data. Finally, for earthquake E4, the MT solution was unstable, with a large difference between the best and mean solutions, and we used the FM solution. In conclusion, we select the MT solutions, except when the polarity score is below 70%. In such case, we select the FM solutions. In Fig. 7, the plotted focal mechanisms correspond to the MT solution (20 events), except for earthquakes E4, E13, E19 and E20 (FM solution). Event 1 has been removed from the selected data.

The distribution of focal mechanisms (Fig. 7) is quite heterogeneous, with mostly dip-slip and normal solutions and few thrust and strike-slip mechanisms. From 20 MT solutions, 9 have a CLVD component lower than 30% (Table 1, events E3–7, E13, E15–16, and E18–21), so the moment tensor solution is dominated by the DC component. A larger CLVD component (greater than 30%) for the remaining 11 earthquakes does not correlate with the magnitude, number of stations or depth. Regarding the stress axes, 7 earthquakes (2 from the FM solution) have a

sub-horizontal P axis (plunge less than 30°), 9 events have sub-horizontal T axes and 5 earthquakes have sub-horizontal T and P axes (E3, E9, E24, E8 and E21) (Table 1).

The MT solution for earthquake E14 is in agreement with the solution obtained by Martín et al. (2015). Solutions for earthquakes E7, E8 and E9 are in agreement with the focal mechanism obtained by Santos-Bueno et al. (2019) using P-wave polarities.

Regarding the other parameters, we obtained M_0 and Mw values (Supplementary Material Table S4). The M_0 values vary from 1.3×10^{13} to 1.9×10^{15} Nm, and the Mw values vary between 2.7 (E6) and 4.2 (E2). We further report Mw values based on mb estimates of the IGN catalog (Supplementary Material Table S2) using the empirical relation by Cabañas et al. (2015) (Supplementary Material Table S2, except for event E14). The M_w values obtained using this relation are generally larger than those obtained by the MT inversion. These results can be explained due to the fact that the relation by Cabañas et al. (2015) was obtained using only shallow earthquakes, not including intermediate-depth earthquakes. An overestimation of the IGN magnitude was also obtained by Santos-Bueno et al. (2019). Our results show that a specific relation between mb and Mw is necessary for intermediate-depth earthquakes for the region.

4. Discussion

From the selected 238 earthquakes (2000−2020), the hypocentral relocation show 227 located have 50 and 100 km focal depth. Eleven earthquakes are shallower (h < 40 km). We find that epicenters and depth uncertainties are larger in the southern Alboran Sea (latitude 35,5°N to 36°N), which we explain as a consequence of the lower station density in Northern Africa (average gap of 173°) and the lower number of picked seismic phases (average of 45 per event). Compared to the original IGN locations, relocated epicenters are shifted slightly to the east; a similar result was also found by Santos-Bueno et al. (2019). A comparison with the locations by Santos-Bueno et al. (2019), which is possible only for 17 common events, suggests a general agreement, except for those earthquakes in which we obtain shallow hypocenters. For the period of 2010–2013, during the temporary deployment of the PICASSO project, we relocated 34 events with magnitudes greater than 3.0; our results are in good agreement with the PICASSO catalog and the locations by Sun and Bezada (2020), except for three earthquakes in northern Morocco, which we found to be shallow, with depths of 24–34 km (Supplementary Material Fig. S8).

Relocations depict a clustered seismicity pattern along an alignment in the western Alboran Sea, with three spatial clusters. The two clusters across the Alboran Sea area are separated by a volume with scarce seismic activity, extending between ~35.8°N and ~ 36.25°N (Fig. 5). The first cluster (A1) extends *E*-W beneath the Spanish coast. The other two clusters (A2 and A3) are located in the western part of the Alboran Sea, with mostly offshore foci distributed in a narrow NNE-SSW strip separated by an aseismic region in the middle of the Alboran Sea. Sun and Bezada (2020), using seismicity data for the period of 1997–2017, proposed the presence of five clusters. They suggest that Cluster A1 is separated into two sub-clusters, but we consider that this separation is hardly resolved, given that the distance between events in the two potential sub-clusters is on the same order of the average location uncertainty. The proposed fifth cluster is in a region where we observe scarce seismic activity; this difference may result from the different criteria applied to select the relocated earthquakes, where we discarded earthquakes with M < 3 and considered the period of 2000–2020.

We obtained the focal mechanism for 24 selected events (4 FM and 20 MT solutions; 15 Quality A and 9 Quality B). Differences in the plunge of the pressure and tension axes of the two solutions are found in few cases and can be explained by the low number of data points or the large amount of CLVD. Relatively large CLVDs are found for a significant number of earthquakes (11 events). Spurious non-double-couple components can appear due to high noise levels in data or network geometry
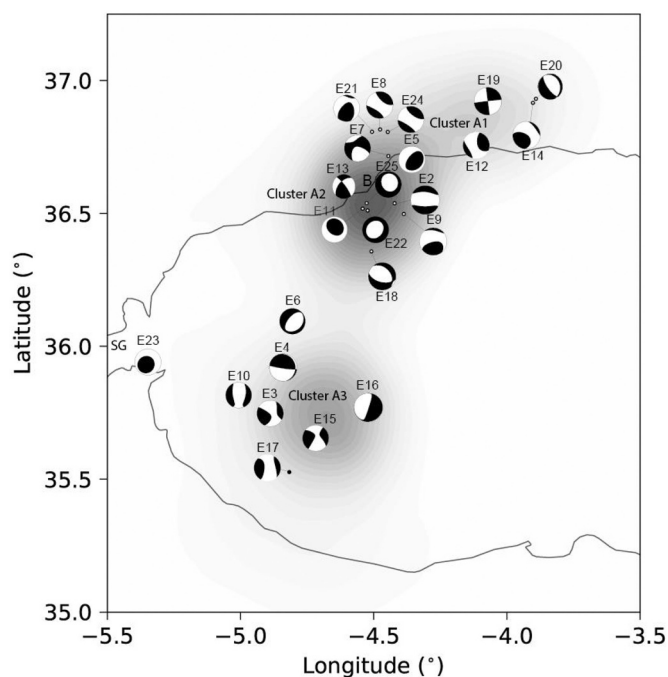

Fig. 7. Focal mechanisms selected from FM and MT solutions (Table 1). The kernel density estimation of epicenters obtained from relocations of this study is represented in grayscale. SG: Strait of Gibraltar.

Table 1

Focal mechanism obtained from MT inversion using *GROND* (Heimann et al., 2018), the asterisk * denotes focal mechanisms from P-wave first-motion (*MECSTA* software, Buforn and Udías, 1984; Udías and Buforn, 1988). REF: event identification; stress trend and plunge; CLVD component (%); strike, dip and rake of fault plane; quality of the solution; score: number of correct observations/total observations.

Ref	Plunge P (°)	Trend P (°)	Plunge T (°)	Trend T (°)	CLVD [%]	Strike [º]	Dip [º]	Rake [º]	Quality	Score [%]
E21	10	287	56	182	15	344	45	40	A	86
E19*	11	132	18	222	–	359	78	14	A	83
E24	10	303	6	34	91	348	87	-12	A	88
E20*	68	41	22	236	–	142	67	−95	A	100
E8	22	304	6	36	79	348	79	−20	A	96
E14	26	337	37	226	69	17	43	11	A	75
E12	21	327	23	66	62	197	89	32	A	82
E7	32	160	9	64	24	197	61	−17	A	100
E5	24	312	65	119	26	53	21	104	A	90
E11	17	228	70	16	62	333	29	111	A	83
E22	84	288	6	131	65	224	39	−86	A	75
E13*	17	88	34	189	–	322	79	38	A	100
E25	73	33	13	256	77	360	34	−70	B	100
E9	41	307	35	180	59	329	30	−7	A	98
E18	70	324	9	209	3	319	39	−62	A	81
E2	83	316	5	183	39	278	40	−82	B	89
E4*	38	199	49	355	–	98	85	102	A	100
E3	18	346	20	249	25	28	62	2	B	80
E17	40	159	17	264	71	207	76	−43	A	100
E10	70	11	3	271	30	164	51	−115	A	100
E6	71	115	18	313	11	52	27	−78	B	75
E15	18	168	13	263	12	215	87	−22	A	100
E16	46	290	44	106	5	125	2	−163	A	93
E23	1	308	68	216	81	17	48	60	B	88

asymmetry (Cesca et al., 2013). The velocity model is likely not responsible for the large CLVDs, as we tested the inversion with different models and similar results (Supplementary Material Figs. S4 and S5). We also found no correlation between the azimuthal coverage and the CLVD percentage, which could suggest a bias due to the network geometry, or between the magnitude and the CLVD percentages, which could indicate a bias due to seismic noise. In these conditions, the non-DC terms may represent a true source feature, either attributed to source complexity (Kagan, 2009) or to the processes driving intermediate-depth seismicity (Frohlich and Nakamura, 2009).

Fig. 7 shows our MT (E2–3, E5–12, E14–18, and E21–25) and FP (E4, E13, E19, and E20) selected solutions (Table 1) and the kernel density estimation of relocated epicenters and the three proposed clusters (A1, A2 and A3). In general, the moment tensor solutions, including their non-DC terms, are quite heterogeneous. Despite this fact, pressure and tension axes are quite homogeneous within each of the three considered clusters. In Cluster A1 (formed by 9 earthquakes), events E19, E12, E24 and E8 have sub-horizontal P and T axes that correspond to strike-slip motion. However, three shocks (E8, E24 and E12) have CLVD components larger than 60% (79%, 91%, and 62%), so we can conclude that in Cluster A1, only E19 (FM solution) has a pure strike-slip mechanism. This earthquake is located inland, with an estimated M_w = 2.8 and depth of 57 km and low hypocenter uncertainties (2 and 1 km for the epicenter and 3 km for depth). These results are in partial disagreement with Santos-Bueno et al. (2019), who suggested an overall predominance of strike-slip solutions. In Cluster A2 (7 events), we observe a predominant sub-horizontal T axis (E22, E25, E18 and E2), with large CLVD components (more than 59% in 4 events) and a clear, stable sub-vertical P axis (Table 1). MTs in Cluster A3 (7 events, namely, E3, E4, E6, E10, E15, E16, and E17) are quite heterogeneous: the southernmost events (E3 and E15) have sub-horizontal P and T axes, denoting a strike-slip component, with variable CLVDs. Event 17 has a sub-horizontal T axis and the largest CLVD of 71%. Events E6 and E10 show sub-vertical P axes, denoting a normal faulting component, and the remaining two events (E4 and E16) show vertical dip-slip mechanisms, with P and T axes dipping approximately 45°. Event 23 (h = 51 km) is located in the SG, and among the concentration of intermediate-depth events, the MT solution has a large CLVD component (81%) and a horizontal P axis.

Fig. 8a shows a horizontal projection of the T axis, and Fig. 8c shows the projection of the P axis. In Fig. 8b and d, we plotted the epicenters of earthquakes with focal mechanisms with symbol sizes proportional to the plunge of the T and P axes, respectively (a vertical axis is represented by a point). The symbol color varies with depth. We observe a predominance of sub-horizontal T axes (plunges less than 30°, Fig. 8a and b). However, their orientations vary substantially from one cluster to the other; a rotation of the trend of this axis varies from a N*E*-SW orientation in Cluster A1 to N-S in Cluster 2 and finally to E-W in Cluster A3. The deepest events (h = 86 to 92 km) are located in Cluster A2. There are fewer earthquakes with a sub-horizontal pressure axis (12 out of 24, Fig. 8c), and generally, the P axis is more regularly NNW-SSE, in agreement with the regional stress regime in this area derived from the convergence between Eurasia and Africa. Only 3 earthquakes have a P axis oriented in the NE-SW to E-W direction, but two of them (E13 and E4 in Clusters A2 and A3, respectively) have FM focal mechanisms, and the third earthquake E11 (MT solution) has a 62% CLVD component. In general, we observe that sub-horizontal NNW-SSE-oriented P axes are characteristic of Cluster A1, north of Cluster A2 and south of Cluster A3. Conversely, events south of Cluster A2 and north of Cluster A3, close to the aseismic region, have a different P axis orientation, which is sub-vertical (Fig. 8d).

Our results do not confirm the predominance of pure strike-slip solutions obtained by Santos-Bueno et al. (2019) based on first-motion polarity. In addition to these differences, we resolve the horizontal compression in the N*E*-SW direction, which is in agreement with the study of Santos-Bueno et al. (2019) and with other previous works in the region (Buforn et al., 1997; Buforn and Coca, 2002; Martín et al., 2015), which is also consistent with the crustal stress field in the Alboran Sea (Stich et al., 2006). However, we point out for the first time a progressive rotation of the tension axes, which are generally sub-horizontal and vary in orientation from EW in the southern Alboran Sea to N*E*-SW on the Spanish coast.

In Fig. 9, we show a scheme of the geometry of the intermediate-depth earthquakes in the Gibraltar Arc. The present position of the emerged Betic-Rif Internal Zones (BIZ and RIF) is result of the WSW wards drift. Consequence of this drift is the sunken slabs of the Iberian and African plates around Gibraltar. The origin of the intermediate-depth earthquakes in the Alboran Sea are this narrow vertical and curved slab, with an asymmetric geometry: more extensive and
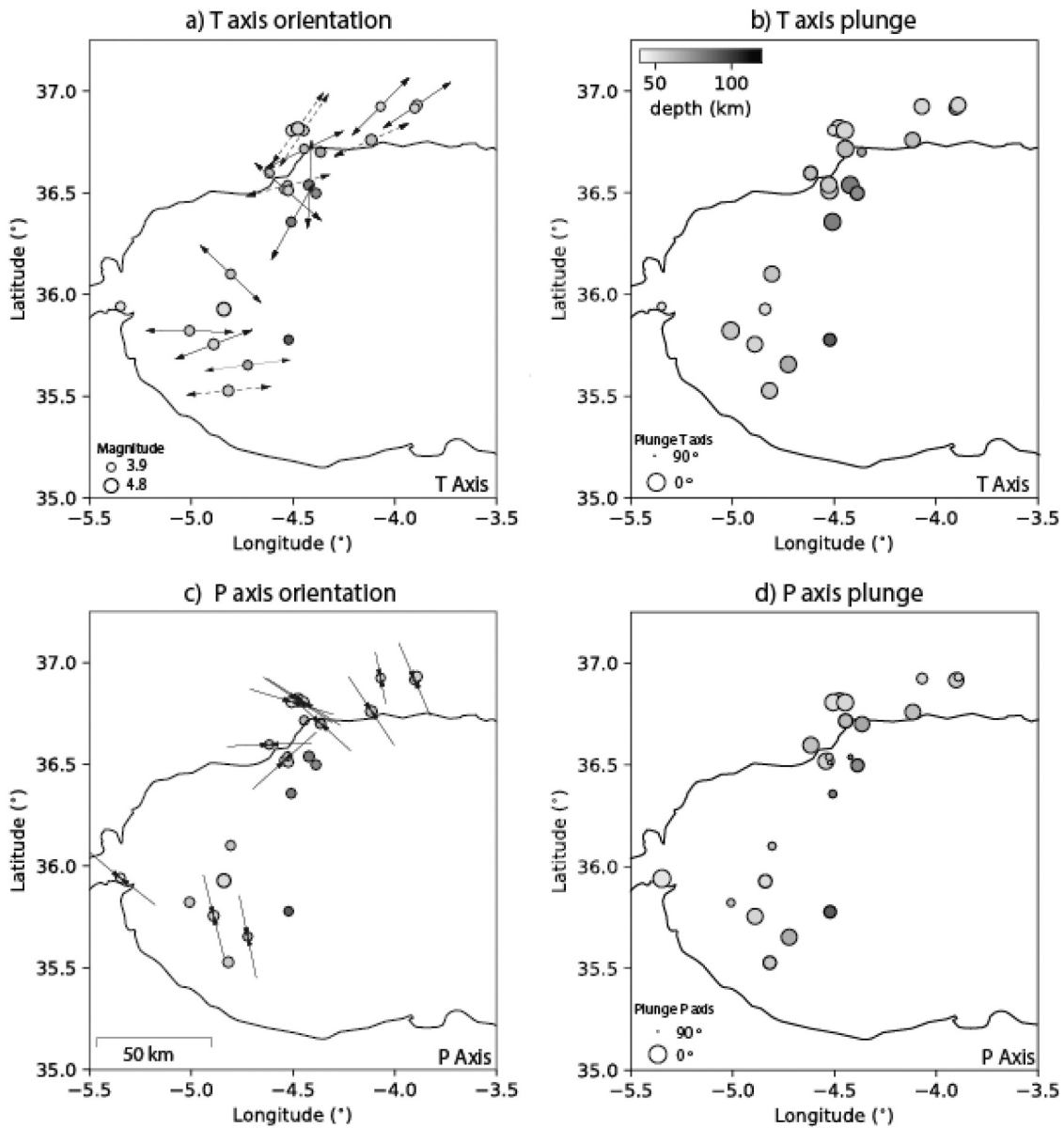
Fig. 8. Left horizontal projections of the T (a) and P (c) axes obtained in this study. Dashed lines represent the solutions with CLVDs greater than 60% and positive values (T axis). At the right plunges of T (8b) and P (8d), the size of the symbol is proportional to the plunge (vertical axes have the minimum size).

developed in the Betic area (Fig. 9). The three clusters of epicenters may be considered the western boundary of the slabs origin by the Internal Zone, defining a transitional region from the base of the crust to the upper part of a slab. Cluster A1 corresponds to the northern part of the boundary region with an E-W region that extends from 40 to 70 km depth and where the stress regime corresponds to NE-SW horizontal extension. Clusters A2 and A3 mark the western part of this transition region, which is deeper than the northern part (extending from 40 km to 110 km). This western part of the slab has a low seismicity region, from 36.25°N to 35.9°N, which is practically a gap, that may be interpreted as the limit between the African and Iberian slabs, a region with different material. There is an abrupt change in the orientation of the T axis across the discontinuity marked by the aseismic region, with horizontal NE-SW extension to the north and E-W extension to the south (Fig. 9). Differences in T axes among clusters are most likely consequence of the slab curvature, rather than with a change in the stress conditions. Intermediate depth seismicity in subducting regions is typically characterized by normal faulting events, striking parallel to the trench. Our results show

very few moment tensor solutions show such a mechanism (only E10 and E6 display a compatible focal mechanism). We interpret this observation as an additional indication of the complexity of the region and that the subduction is not active (Pedrera et al., 2011; Buforn et al., 2016; Sun and Bezada, 2020). Thus, the seismicity occurs within the volume of the inactive subduction, but is controlled by other tectonic stresses, such as the aforementioned Iberian-African convergence.

Other authors, such as Sun and Bezada (2020), have associated this intermediate-depth seismicity with delamination and thinning of the slab, as tomography is unable to resolve it. According to their model, Clusters A2 and A3 (extending within 40–110 km depth in the NE-SW orientation; Fig. 8a) would be located on and inside the slab (Bezada et al., 2014; Bonnin et al., 2014; Monna et al., 2013; Villaseñor et al., 2015). The seismicity in the slab (h > 60 km) has been interpreted by Heit et al. (2017) as a consequence of an N-S sub-horizontal plane tear of the slab. Our study shows a progressive change in the orientation of the extensional stress from NE-SW in southern Iberia to E-W in northern Africa (Fig. 8a). The extensional stresses are perpendicular to the
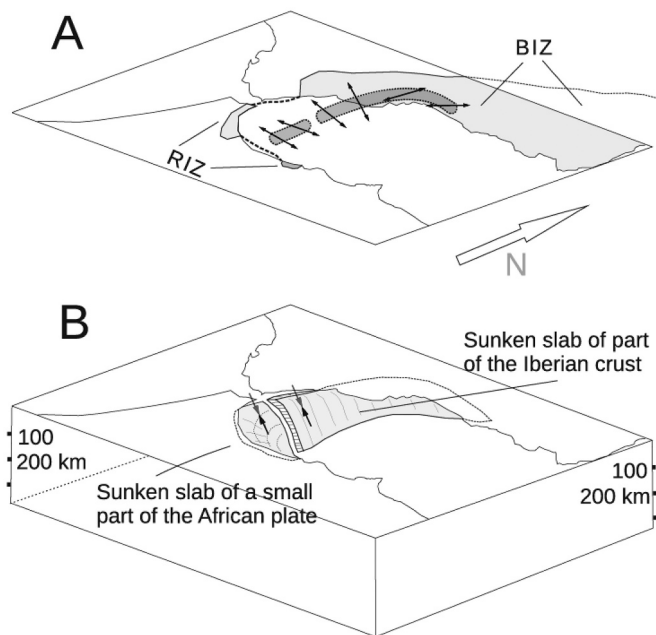
Fig. 9. Schematic reconstruction of the geometry of the subduction in the Gibraltar arc. A: present position of the emerged Betic-Rif Internal Zone (BIZ-RIZ) along with a schematic of the seismicity and the horizontal projections of the T axes. B: the sunken slabs of the Iberian and African plates along with a schematic of the vertical projections P axes.

borders of the slab, both at the Gibraltar Arc and the southern coast of Spain. The NW-SE horizontal compression at the southern coast of Spain (Fig. 8c) derived from our focal mechanism may be explained in terms of the convergence between Eurasia and Africa. The vertical compression in Clusters A2 and A3 is more difficult to explain, may be consequence of this former "composed" subduction, and it is an evidence of the tectonic complexity of this region.

The intermediate-depth seismicity is not correlated to the shallow earthquakes that occurred in the Alboran Sea, which are located east of the intermediate-depth events, following a NE-SW direction, from Almeria in southern Spain to Al Hoceima in northern Africa (Fig. 3) and with focal mechanism of strike-slip motion. Furthermore, another evidence of the complex seismotectonic of this area nor is the correlation between the intermediate and the very deep seismicity located in a nest at the bottom of the slab (at a depth of approximately 650 km) under Granada and where the focal mechanisms correspond to P and T axes oriented E-W and dipping 45° (Buforn et al., 1991, 2011).

5. Conclusions

The results of the relocation of 227 intermediate-depth hypocenters that occurred in the Alboran Sea between 2000 and 2020, using a nonlinear method (NNL) and a 3D-velocity model show that the seismicity extends laterally in the western part of the Alboran Sea almost parallel to the Gibraltar Arc in a narrow band of ~50 km between 40 and 110 km depth. The use of a 3D earth model takes in account the tectonic complexity of the region, thereby improving the quality of the hypocenters. We observe a slight displacement toward the east of the hypocenters compared to the IGN catalog.

Three clusters of earthquakes are observed, one in an E-W orientation in southern Spain and two offshore N-S orientations separated by a seismic gap, in the limit between the African and Iberian slabs. The focal depth increases from the Strait of Gibraltar, reaching a maximum (110 km) at 4.5°W and it is lower in the northeast (onshore epicenters in southern Spain).

Focal mechanisms and moment tensors of 24 earthquakes were obtained using P-wave first-motion and waveforms and amplitude spectra moment tensor inversion. In the last case, we repeated the MT inversion with two different 1-D velocity models, obtaining similar results. In 11 cases, the CLVD component of the MT inversion is greater than 30%, a percentage that may represent a true source feature, either attributed to a source complexity or to the processes driving intermediate-depth seismicity. Focal mechanism solutions are heterogeneous, but we identify clear spatial patterns in their principal axis orientation. Pressure axes are either oriented NW-SE, compatible with plate convergence, or sub-vertical, in the central part of the Alboran Sea. Predominant horizontal extension stresses show a rotation from NE-SW in southern Spain to E-W in northern Africa. We found no clear relation among the intermediate-depth seismicity and the shallow and very deep earthquakes also present in this region.

Declaration of Competing Interest

None.

Appendix A. Supplementary data

Supplementary data to this article can be found online at https://doi.org/10.1016/j.tecto.2022.229238.

References

Aït Brahim, L., Nakhcha, C., Tadili, B., El Mrabet, A., Jabour, N., 2004. Structural analysis and interpretation of the surface deformations of the February 24th, 2004 Al Hoceima earthquake. Newsletter 21, 10–12. Eur.-Mediter. Seismol. Cent., Bruyères-le-Châtel, France.

Amaru, M.L., 2007. Global Travel Time Tomography with 3-D Reference Models, vol. 274. Utrecht University.

Andrieux, J., Fontboté, J.M., Mattauer, M., 1971. Sur un modele explicative de l'Arc de Gibraltar. Earth Planet. Sci. Lett. 12, 191–198. https://doi.org/10.1016/0012-821X(71)90077-X.

Bassin, C., Laske, G., Masters, G., 2000. The current limits of resolution for surface wave tomography in North America. EOS, Trans. Am. geophys. Un. 81, F897.

Bezada, M.J., Humphreys, E.D., 2012. Contrasting rupture processes during the April 11, 2010 deep-focus earthquake beneath Granada, Spain. Earth Planet. Sci. Lett. 353, 38–46. https://doi.org/10.1016/j.epsl.2012.08.001.

Bezada, M.J., Humphreys, E.D., Toomey, D.R., Harnafi, M., Dávila, J.M., Gallart, J., 2013. Evidence for slab rollback in westernmost Mediterranean from improved upper mantle imaging. Earth Planet. Sci. Lett. 368, 51–60. https://doi.org/10.1016/j.epsl.2013.02.024.

Bezada, M.J., Humphreys, E.D., Davila, J.M., Carbonell, R., Harnafi, M., Palomeras, I., Levander, A., 2014. Piecewise delamination of Moroccan lithosphere from beneath the Atlas Mountains. Geochem. Geophys. Geosyst. 15 (4), 975–985. https://doi.org/10.1002/2013GC005059.

Blanco, M.J., Spakman, W., 1993. The P-wave velocity structure of the mantle below the Iberian Peninsula: evidence for subducted lithosphere below southern Spain. Tectonophysics 221 (1), 13–34. https://doi.org/10.1016/0040-1951(93)90025-F.

Bonnin, M., Nolet, G., Villasenor, A., Gallart, J., Thomas, C., 2014. Multiple-frequency tomography of the upper mantle beneath the African/Iberian collision zone. Geophys. J. Int. 198 (3), 1458–1473. https://doi.org/10.1093/gji/ggu214.

Bratt, S.R., Bache, T.C., 1988. Locating events with a sparse network of regional arrays. Bull. Seismol. Soc. Am. 78 (2), 780–798. https://doi.org/10.1785/BSSA0780020780.

Brillinger, D.R., Udías, A., Bolt, B.A., 1980. A probability model for regional focal mechanism solutions. Bull. Seismol. Soc. Am. 70 (1), 149–170. https://doi.org/10.1785/BSSA0700010149.

Buforn, E., Coca, P., 2002. Seismic moment tensor for intermediate depth earthquakes at regional distances in Southern Spain. Tectonophysics 356 (1–3), 49–63. https://doi.org/10.1016/S0040-1951(02)00376-1.

Buforn, E., Udías, A., 1984. An algorithm for focal mechanism determination using signs of first motion of P, SV and SH waves. Rev de Geofisica 40, 11–26.

Buforn, E., Udías, A., Colombás, M.A., 1988a. Seismicity, source mechanisms and Tectonics of the Azores-Gibraltar plate boundary. Tectonophysics 152 (1–2), 89–118. https://doi.org/10.1016/0040-1951(88)90031-5.

Buforn, E., Udías, A., Mezcua, J., 1988b. Seismicity and focal mechanisms in South Spain. Bull. Seismol. Soc. Am. 78 (6), 2008–2024. https://doi.org/10.1785/BSSA0780062008.

Buforn, E., Udías, A., Mezcua, J., Madariaga, R., 1991. A deep earthquake under south Spain, 8 March 1990. Bull. Seismol. Soc. Am. 81 (4), 1403–1407.

Buforn, E., Sanz de Galdeano, C., Udías, A., 1995. Seismotectonics of the Ibero-Maghrebian region. Tectonophysics 248 (3–4), 247–261. https://doi.org/10.1016/0040-1951(94)00276-F.

Buforn, E., Coca, P., Udías, A., Lasa, C., 1997. Source mechanism of intermediate and deep earthquakes in southern Spain. J. Seismol. 1 (2), 113–130. https://doi.org/10.1023/A:1009754219459.

Buforn, E., Pro, C., Cesca, S., Udías, A., Del Fresno, C., 2011. The 2010 Granada, Spain, deep earthquake. Bull. Seismol. Soc. Am. 101 (5), 2418–2430. https://doi.org/10.1785/0120110022.

Buforn, E., Udías, A., Pro, C., 2016. Source mechanism studies of earthquakes in the Ibero-Maghrebian region and their tectonic implications. J. Seismol. 20 (4), 1075–1088. https://doi.org/10.1007/s10950-015-9551-7.

Buforn, E., Pro, C., Sanz de Galdeano, C., Cantavella, J.V., Cesca, S., Caldeira, B., Udías, A., Mattesini, M., 2017. The 2016 south Alboran earthquakes (Mw=6.4): a reactivation of the Ibero-Maghrebian region? Tectonophysics 712-713, 704–715. https://doi.org/10.1016/j.tecto.2017.06.033.

Cabañas, L., Rivas-Medina, A., Martínez-Solares, J.M., Gaspar-Escribano, J.M., Benito, B., Antón, R., Ruiz-Barajas, S., 2015. Relationships between Mw and other earthquake size parameters in the Spanish IGN seismic catalog. Pure Appl. Geophys. 172 (9) https://doi.org/10.1007/s00024-014-1025-2.

Cabieces, R., Buforn, E., Cesca, S., Pazos, A., 2020. Focal parameters of earthquakes offshore Cape St. Vincent using an amphibious network. Pure Appl. Geophys. 177 (4), 1761–1780. https://doi.org/10.1007/s00024-020-02475-3.

Calvert, A., Sandvol, E., Seber, D., Barazangi, M., Roecker, S., Mourabit, T., Jabour, N., 2000. Geodynamic evolution of the lithosphere and upper mantle beneath the Alboran region of the western Mediterranean: Constraints from travel time tomography. J. Geophys. Res. Solid Earth 105 (B5), 10871–10898. https://doi.org/10.1029/2000JB900024.

Carminati, E., Lustrino, M., Doglioni, C., 2012. Geodynamic evolution of the central and western Mediterranean: *Tectonics* vs. igneous petrology constraints. Tectonophysics 579, 173–192. https://doi.org/10.1016/j.tecto.2012.01.026.

Casado, C.L., Sanz de Galdeano, C., Molina, S., Henares, J., 2001. The structure of the Alboran Sea: an interpretation from seismological and geological data. Tectonophysics 338, 79–95. https://doi.org/10.1016/S0040-1951(01)00059-2.

Cesca, S., Rohr, A., Dahm, T., 2013. Discrimination of induced seismicity by full moment tensor inversion and decomposition. J. Seismol. 17 (1), 147–163. https://doi.org/10.1007/s10950-012-9305-8.

Cesca, S., Stich, D., Grigoli, F., Vuan, A., López-Comino, J.Á., Niemz, P., Ellsworth, W.L., 2021. Seismicity at the Castor gas reservoir driven by pore pressure diffusion and asperities loading. Nat. Commun. 12 (1), 1–13. https://doi.org/10.1038/s41467-021-24949-1.

Chung, W.Y., Kanamori, H., 1976. Source process and tectonic implications of the Spanish deep-focus earthquake of March 29, 1954. Phys. Earth Planet. Inter. 13 (2), 85–96. https://doi.org/10.1016/0031-9201(76)90073-X.

de Lamotte, D.F., Leturmy, P., Missenard, Y., Khomsi, S., Ruiz, G., Saddiqi, O., Michard, A., 2009. Mesozoic and Cenozoic vertical movements in the Atlas system (Algeria, Morocco, Tunisia): an overview. Tectonophysics 475 (1), 9–28. https://doi.org/10.1016/j.tecto.2008.10.024.

Domingues, A., Custodio, S., Cesca, S., 2013. Waveform inversion of small-to-moderate earthquakes located offshore Southwest Iberia. Geophys. J. Int. 192 (1), 248–259. https://doi.org/10.1093/gji/ggs010.

El Moudnib, L., Villaseñor, A., Harnafi, M., Gallart, J., Pazos, A., Serrano, I., et al., 2015. Crustal structure of the Betic–Rif system, western Mediterranean, from local earthquake tomography. Tectonophysics 643, 94–105. https://doi.org/10.1016/j.tecto.2014.12.015.

Frohlich, C., Nakamura, Y., 2009. The physical mechanisms of deep moonquakes and intermediate-depth earthquakes: how similar and how different? Phys. Earth Planet. Inter. 173 (3–4), 365–374. https://doi.org/10.1016/j.pepi.2009.02.004.

Galindo-Zaldívar, J., Ercilla, G., Estrada, F., Catalán, M., d'Acremont, E., Azzouz, O., Gil, A.J., 2018. Imaging the growth of recent faults: the case of 2016–2017 seismic sequence sea bottom deformation in the Alboran Sea (Western Mediterranean). Tectonics 37 (8), 2513–2530. https://doi.org/10.1029/2017TC004941.

Gómez de la Peña, L., Ranero, C.R., Gràcia, E., 2018. The crustal domains of the Alboran Basin (western Mediterranean). Tectonics 37, 3352–3377. https://doi.org/10.1029/2017TC004946.

Gràcia, E., Grevemeyer, I., Bartolomé, R., Perea, H., Martínez-Loriente, S., Gómez de la Peña, L., Ranero, C.R., 2019. Regional centroid moment tensors for earthquakes in the 2016 South Alboran seismic crisis. https://doi.org/10.20350/digitalCSIC/8623.

Grimison, N.L., Chen, W.P., 1986. The Azores-Gibraltar plate boundary: Focal mechanisms, depths of earthquakes, and their tectonic implications. J. Geophys. Res. Solid Earth 91 (B2), 2029–2047. https://doi.org/10.1029/JB091iB02p02029.

Gutscher, M.A., Malod, J., Rehault, J.P., Contrucci, I., Klingelhoefer, F., Mendes-Victor, L., Spakman, W., 2002. Evidence for active subduction beneath Gibraltar.

Geology 30 (12), 1071–1074. https://doi.org/10.1130/0091-7613(2002)030<1071:EFASBG>2.0.CO;2.

Gutscher, M.A., Dominguez, S., Westbrook, G.K., Le Roy, P., Rosas, F., Duarte, J.C., Bartolomé, R., 2012. The Gibraltar subduction: a decade of new geophysical data. Tectonophysics 574, 72–91. https://doi.org/10.1016/j.tecto.2012.08.038.

Hatzfeld, D., 1978. *Etude sismotectonique de la zone de collision Ibero-Maghrebine* (Doctoral dissertation, Université Scientifique et Médicale de Grenoble).

Hatzfeld, D., Frogneux, M., 1981. Intermediate depth seismicity in the western Mediterranean unrelated to subduction of oceanic lithosphere. Nature 292 (5822), 443–445. https://doi.org/10.1038/292443a0.

Heimann, S., Isken, M., Kühn, D., Sudhaus, H., Steinberg, A., Daout, S., Dahm, T., 2018. Grond: A Probabilistic Earthquake Source Inversion Framework, V. 1.0. GFZ Data Services. https://doi.org/10.5880/GFZ.2.1.2018.003.

Heit, B., Mancilla, F.d.L., Yuan, X., Morales, J., Stich, D., Martín, R., Molina-Aguilera, A., 2017. Tearing of the mantle lithosphere along the intermediate-depth seismicity zone beneath the Gibraltar Arc: the onset of lithospheric delamination. Geophys. Res. Lett. 44 (9), 4027–4035. https://doi.org/10.1002/2017GL073358.

Hensch, M., Dahm, T., Ritter, J., Heimann, S., Schmidt, B., Stange, S., Lehmann, K., 2019. Deep low-frequency earthquakes reveal ongoing magmatic recharge beneath Laacher See Volcano (Eifel, Germany). Geophys. J. Int. 216 (3), 2025–2036. https://doi.org/10.1093/gji/ggy532.

Hodgson, J.H., Cock, J.I., 1956. Direction of faulting in the deep-focus Spanish earthquake of March 29, 1954. Tellus 8 (3), 321–328. https://doi.org/10.3402/tellusa.v8i3.9020.

Instituto Geográfico Nacional (IGN), 2021. The Spanish seismic catalog, IGN – Instituto Geográfico Nacional. Catálogo Sísmico Nacional. available at. http://www.ign.es (last access date: September 2021).

Jabour, N., Kasmi, M., Menzhi, M., Birouk, A., Hni, L., Hahou, Y., Timoulali, Y., Badrane, S., 2004. The February 24th, 2004 Al Hoceima earthquake. Newsletter 21, 7–10. Eur.-Méditer. Seismol. Cent., Bruyères-le-Châtel, France.

Kagan, Y.Y., 2009. On the geometric complexity of earthquake focal zone and fault systems: a statistical study. Phys. Earth Planet. Inter. 173 (3–4), 254–268. https://doi.org/10.1016/j.pepi.2009.01.006.

Kariche, J., Meghraoui, M., Timoulali, Y., Cetin, E., Toussaint, R., 2018. The Al Hoceima earthquake sequence of 1994, 2004 and 2016: stress transfer and poroelasticity in the Rif and Alboran Sea region. Geophys. J. Int. 212 (1), 42–53. https://doi.org/10.1093/gji/ggx385.

Kennett, B.L.N., Engdahl, E.R., 1991. Traveltimes for global earthquake location and phase identification. Geophys. J. Int. 105 (2), 429–465. https://doi.org/10.1111/j.1365-246X.1991.tb06724.x.

Levander, A., Bezada, M.J., Niu, F., Humphreys, E.D., Palomeras, I., Thurner, S.M., Miller, M.S., 2014. Subduction-driven recycling of continental margin lithosphere. Nature 515 (7526), 253–256. https://doi.org/10.1038/nature13878.

Lomax, A., 2005. A reanalysis of the hypocentral location and related observations for the great 1906 California earthquake. Bull. Seismol. Soc. Am. 95 (3), 861–877. https://doi.org/10.1785/0120040141.

Lomax, A., Curtis, A., 2001. Fast, probabilistic earthquake location in 3D models using oct-tree importance sampling. Geophys. Res. Abstr. 3, 955.

Lomax, A., Virieux, J., Volant, P., Berge-Thierry, C., 2000. Probabilistic earthquake location in 3D and layered models. In: Thurber, C.H., Rabinowitz, N. (Eds.), Advances in Seismic Event Location. Modern Approaches in Geophysics, Vol 18. Springer, Dordrecht. https://doi.org/10.1007/978-94-015-9536-0_5.

Lozano, L., Cantavella, J.V., Barco, J., 2020. A new 3-D P-wave velocity model for the Gulf of Cadiz and adjacent areas derived from controlled-source seismic data: application to non-linear probabilistic relocation of moderate earthquakes. Geophys. J. Int. 221 (1), 1–19. https://doi.org/10.1093/gji/ggz562.

Mancilla, F.d.L., Stich, D., Morales, J., Julià, J., Diaz, J., Pazos, A., Gonzalez-Lodeiro, F., 2012. Crustal thickness variations in northern Morocco. J. Geophys. Res. Solid Earth 117 (B2). https://doi.org/10.1029/2011JB008608.

Mancilla, F.d.L., Stich, D., Berrocoso, M., Martín, R., Morales, J., Fernandez-Ros, A., Pérez-Peña, A., 2013. Delamination in the betic range: deep structure, seismicity, and GPS motion. Geology 41 (3), 307–310. https://doi.org/10.1130/G33733.1.

Martín, R., Stich, D., Morales, J., Mancilla, F.d.L., 2015. Moment tensor solutions for the Iberian-Maghreb region during the IberArray deployment (2009–2013). Tectonophysics 663, 261–274. https://doi.org/10.1016/j.tecto.2015.08.012.

Martínez-Solares, J.M., 1995. Boletín de sismos próximos 1995. IGN, Madrid, p. 13.

Medina, F., Cherkaoui, T.E., 2017. The south-western Alboran earthquake sequence of January-March 2016 and its associated coulomb stress changes. Open J. Earthq. Res 6 (01), 35. https://doi.org/10.4236/ojer.2017.61002.

Mezcua, J., Rueda, J., 1997. Seismological evidence for a delamination process in the lithosphere under the Alboran Sea. Geophys. J. Int. 129 (1), F1–F8. https://doi.org/10.1111/j.1365-246X.1997.tb00934.x.

Monna, S., Cimini, G.B., Montuori, C., Matias, L., Geissler, W.H., Favali, P., 2013. New insights from seismic tomography on the complex geodynamic evolution of two adjacent domains: Gulf of Cadiz and Alboran Sea. J. Geophys. Res. Solid Earth 118 (4), 1587–1601. https://doi.org/10.1029/2012JB009607.

Morales, J., Serrano, I., Jabaloy, A., Galindo-Zaldívar, J., Zhao, D., Torcal, F., Vidal, F., González Lodeiro, F., 1999. Active continental subduction beneath the Betic Cordillera and the Alborán Sea. Geology 27 (8), 735–738. https://doi.org/10.1130/0091-7613(1999)027<0735:ACSBTB>2.3.CO;2.

Munuera, J.M., 1963. Datos básicos para un estudio de sismicidad en el área de la península Ibérica (Seismic data) *Mem. Instituto Geográfico Catastral XXII* (Madrid).

Palomeras, I., Thurner, S., Levander, A., Liu, K., Villaseñor, A., Carbonell, R., Harnafi, M., 2014. Finite-frequency Rayleigh wave tomography of the western Mediterranean: mapping its lithospheric structure. Geochem. Geophys. Geosyst. 15 (1), 140–160. https://doi.org/10.1002/2013GC004861.

Pedrera, A., Ruiz-Constán, A., Galindo-Zaldívar, J., Chalouan, A., Sanz de Galdeano, C., Marín-Lechado, C., Ruano, P., Benmakhlouf, M., Akil, M., López-Garrido, A.C., Chabli, A., Ahmamou, M., González-Castillo, L., 2011. Is there an active subduction beneath the Gibraltar orogenic arc? Constraints from Pliocene to present-day stress field. J. Geodyn. 52 (2), 83–96. https://doi.org/10.1016/j.jog.2010.12.003.

Piromallo, C., Morelli, A., 2003. P wave tomography of the mantle under the Alpine-Mediterranean area. J. Geophys. Res. Solid Earth 108 (B2). https://doi.org/10.1029/2002JB001757.

Platt, J.P., Vissers, R.L.M., 1989. Extensional collapse of thickened continental lithosphere: a working hypothesis for the Alboran Sea and Gibraltar arc. Geology 17 (6), 540–543. https://doi.org/10.1130/0091-7613(1989)017<0540: ECOTCL>2.3. CO;2.

Podvin, P., Lecomte, I., 1991. Finite-difference computation of traveltimes in very contrasted velocity models - a massively parallel approach and it associated tools. Geophys. J. Int. 105 (1), 271–284. https://doi.org/10.1111/j.1365-246X.1991.tb03461.x.

Santos-Bueno, N., Fernández-García, C., Stich, D., Mancilla, F.d.L., Martín, R., Molina-Aguilera, A., Morales, J., 2019. Focal mechanisms for subcrustal earthquakes beneath the Gibraltar Arc. Geophys. Res. Lett. 46 (5), 2534–2543. https://doi.org/10.1029/20lom18GL081587.

Sanz de Galdeano, C., 1990. Geologic evolution of the Betic Cordilleras in the Western Mediterranean, Miocene to the present. Tectonophysics 172, 107–119. https://doi.org/10.1016/0040-1951(90)90062-D.

Seber, D., Barazangi, M., Ibenbrahim, A., Demnati, A., 1996. Geophysical evidence for lithospheric delamination beneath the Alboran Sea and Rif–Betic mountains. Nature 379 (6568), 785–790. https://doi.org/10.1038/379785a0.

Spakman, W., Wortel, R., 2004. A tomographic view on western Mediterranean geodynamics. In: The TRANSMED Atlas. *The Mediterranean Region from Crust to Mantle*. Springer, Berlin, Heidelberg, pp. 31–52. https://doi.org/10.1007/978-3-642-18919-7_2.

Stich, D., Ammon, C.J., Morales, J., 2003. Moment tensor solutions for small and moderate earthquakes in the Ibero-Maghreb region. J. Geophys. Res. Solid Earth 108 (B3). https://doi.org/10.1029/2002JB002057.

Stich, D., Mancilla, F.d.L., Baumont, D., Morales, J., 2005. Source analysis of the Mw 6.3 2004 Al Hoceima earthquake (Morocco) using regional apparent source time functions. J. Geophys. Res. Solid Earth 110 (B6). https://doi.org/10.1029/2004JB003366.

Stich, D., Serpelloni, E., Mancilla, F.d.L., Morales, J., 2006. Kinematics of the Iberia–Maghreb plate contact from seismic moment tensors and GPS observations. Tectonophysics 426 (3–4), 295–317. https://doi.org/10.1016/j.tecto.2006.08.004.

Stich, D., Martín, R., Morales, J., López-Comino, J.Á., Mancilla, F.d.L., 2020. Slip partitioning in the 2016 alboran sea earthquake sequence (western mediterranean). Front. Earth Sci. https://doi.org/10.3389/feart.2020.587356.

Sun, M., Bezada, M., 2020. Seismogenic necking during slab detachment: evidence from relocation of intermediate-depth seismicity in the Alboran slab. J. Geophys. Res. Solid Earth 125. https://doi.org/10.1029/2019JB017896 e2019JB017896.

Tarantola, A., Valette, B., 1982. Generalized non-linear inverse problems solved using the least-squares criterion. Rev. Geophys. 20 (2), 219–232. https://doi.org/10.1029/RG020i002p00219.

Udías, A., Buforn, E., 1988. Single and joint fault-plane solutions from first motion data. In: Doornbos, D.J. (Ed.), Seismological Algorithms. Academic Press, New York, pp. 443–453.

Udías, A., López-Arroyo, A., 1972. Plate tectonics and the Azores-Gibraltar region. Nature 237, 67–69. https://doi.org/10.1038/physci237067a0.

Udías, A., López-Arroyo, A., Mezcua, J., 1976. Seismotectonic of the Azores-Alboran region. Tectonophysics 31 (3–4), 259–289. https://doi.org/10.1016/0040-1951(76)90121-9.

Van Hinsbergen, D.J., Vissers, R.L., Spakman, W., 2014. Origin and consequences of western Mediterranean subduction, rollback, and slab segmentation. Tectonics 33 (4), 393–419. https://doi.org/10.1002/2013TC003349.

Vergés, J., Fernàndez, M., 2012. Tethys–Atlantic interaction along the Iberia–Africa plate boundary: The Betic–Rif orogenic system. Tectonophysics 579, 144–172. https://doi.org/10.1016/j.tecto.2012.08.032.

Villaseñor, A., Chevrot, S., Harnafi, M., Gallart, J., Pazos, A., Serrano, I., Ibarra, P., 2015. Subduction and volcanism in the Iberia–North Africa collision zone from tomographic images of the upper mantle. Tectonophysics 663, 238–249. https://doi.org/10.1016/j.tecto.2015.08.042.

Wadati, K., 1933. On the Travel Time of Earthquake Waves. Part. II. *Geophys. Mag.* (Tokyo) 7, 101–111. https://doi.org/10.2151/jmsj1923.11.1_14.

Walter, T.R., Haghighi, M.H., Schneider, F.M., Coppola, D., Motagh, M., Saul, J., Gaebler, P., 2019. Complex hazard cascade culminating in the Anak Krakatau sector collapse. Nat. Commun. 10 (1), 1–11. https://doi.org/10.1038/s41467-019-12284-5.

Wang, R., 1999. A simple orthonormalization method for stable and efficient computation of Green's functions. Bull. Seismol. Soc. Am. 89 (3), 733–741. https://doi.org/10.1785/BSSA0890030733.